Quantitative characterization of built-in potential profile across GaAs p-n junctions using Kelvin probe force microscopy with qPlus sensor AFM

Nobuyuki Ishida

National Institute for Materials Science, 1-2-1 Sengen, Tsukuba, Ibaraki 305-0047, Japan

E-mail: ishida.nobuyuki@nims.go.jp

Takaaki Mano

National Institute for Materials Science, 1-2-1 Sengen, Tsukuba, Ibaraki 305-0047, Japan

August 2017

Abstract. The electrostatic potential distribution in materials and devices plays an important role in controlling the behaviors of charge carriers. Kelvin probe force microscopy (KPFM) is a powerful technique for measuring the surface potential at a high spatial resolution. However, the measured surface potential often deviates from the potential deep in the bulk owing to certain factors. Here, we performed KPFM measurements across the p-n junction, in which such factors were eliminated as much as possible by selecting the sample, force sensor, and measurement mode. The measured surface potential distribution agrees well with the line shape of the simulated bulk potential. Our results demonstrate that KPFM is capable of quantitatively characterizing potential distributions whose changes occur on the order of 10 nm.

1. Background

Kelvin probe force microscopy (KPFM) is a technique for measuring the work function and electrostatic potential of a surface by detecting the contact potential difference (CPD) between the tip and the sample [1, 2, 3, 4]. Since its invention, KPFM has been used to evaluate various electronic [3, 5, 6, 7, 8, 9, 10, 11, 12, 13] and ionic devices [14, 15, 16, 17, 18, 19]. In particular, several reports have focused on the characterization of the built-in potential profiles in p-n junctions [5, 20, 8, 21, 22, 9, 11, 12], which are the key components of semiconductor devices. However, the magnitudes of the measured built-in potentials are smaller than those expected from the actual band structure. There are two primary reasons for this discrepancy. The first is related to the fact that KPFM measures the surface potential. In general, the surface potential is different from the potential deep in the bulk owing to surface band bending arising from surface

reconstruction, defects, surface oxidation, etc. [23, 24] The other is the tip-averaging effect [25, 26, 27, 28]. The CPD measured by KPFM is a weighted average of the surface potential underneath the tip apex because of the long-range nature of the electrostatic force acting between the tip and sample. It is generally difficult to compensate for these effects for arbitrary samples. These issues have prohibited the direct comparison of CPD profiles with the simulated bulk potentials of specimens with continuously varying potential distributions on the nanometer-scale, such as p-n junctions in semiconductor devices.

KPFM is a derivative of atomic force microscopy (AFM). Most of the device characterizations using KPFM use the cantilever-based optical lever method [5, 20, 6, 7, 8, 21, 29, 30, 9, 10, 11, 13]. When a cantilever is used, the averaging effect is caused not only by the tip apex and cone but also by the metal film coated on the cantilever [27]. In contrast, in AFM using a tuning fork type force sensor (qPlus sensor) [31, 32], no large metallic part comes closer to the surface except for a relatively long sharp metal tip. Thus, the tip-averaging effect is expected to be smaller than when using cantilever-type AFM.

In this study, we performed KPFM using a qPlus sensor AFM to measure the well-defined potential distribution formed across the GaAs p-n junction, where most of the potential change occurs within the range of approximately 50 nm. The measurements were performed on a step-free GaAs(110) surface with a flat band from the bulk to the surface [23, 33]. This enabled us to analyze the bulk potential distribution via surface potential measurements. Under these ideal conditions, we verified the quantitativity of the KPFM measurements. We show that the use of higher-order polynomials instead of a 2nd-order polynomial (a quadratic function) in the fitting procedure during CPD derivation improves the accuracy of the CPD measurements. The CPD profiles obtained by the fittings coincided well with the line shape of the simulated potential distribution. Our results demonstrate that KPFM can quantitatively measure the potential distribution as long as the change in the potential distribution occurs on the order of 10 nm. We also show that the use of one-dimensional (1D) tunneling spectroscopy together with KPFM is a powerful way to characterize band structures in semiconductor devices in detail.

2. Methods

2.1. Sample preparation and characterization

We fabricated GaAs p-n junctions on n-type GaAs(001) substrates using solid-source molecular beam epitaxy. First, we grew a 300 nm thick n-GaAs (Si doped, $N_{\mathrm{D}} = 1\times10^{18}$ cm^{-3}) buffer layer at a substrate temperature of 580 °C. Subsequently, p-n junction layers consisting of 600 nm thick n-GaAs (Si doped, $N_{\mathrm{D}} = 5 \times 10^{17}$ cm^{-3}) and 600 nm thick p-GaAs (Be doped, $N_{\mathrm{A}} = 5 \times 10^{17}$ cm^{-3}) were deposited. Finally, we grew a 300 nm thick p^{+}-GaAs (Be doped, $N_{\mathrm{A}} = 2 \times 10^{19}$ cm^{-3}) layer. An alloyed AuGe/Ni/Au

electrode was fabricated on the substrate side for the ohmic contact. For the surface, the ohmic behavior was obtained by contacting the surface with the metal part of the sample holder due to the high doping concentration of the p^+-GaAs layer.

The diode properties of the device and its open-circuit voltage (OCV) were evaluated by measuring the current-voltage characteristics in dark and under light irradiation conditions, respectively. The measurements were performed using a source measure unit (ADCMT, 6241A) at 78 K under the ultrahigh vacuum (UHV) conditions. A laser diode (635 nm) was used as the light source. The total power of the laser was 0.95 mW, and the roughly estimated diameter of the laser spot was 2 mm. The laser light was introduced into the UHV chamber through a viewing port. The theoretical potential profile across the p-n junction was calculated using SEMITIP software version 6 developed by Feenstra [34].

2.2. STM and AFM measurements

. Scanning tunneling microscopy (STM) and AFM measurements were performed at 78 K under UHV conditions ($< 1 \times 10^{-8}$ Pa) using a low-temperature scanning probe microscopy (SPM) system (Unisoku USM-1400). The qPlus sensors with electrochemically etched tungsten (W) tips were used. The typical resonance frequency of the sensor ranged from 24 to 31 kHz. The surface oxide layers on the W tips were removed by Ar^+-ion sputtering (1.5 kV) for 20 min, and the tip apex was conditioned on clean Au(111) surfaces prior to the experiments. The forces acting between the tip and sample were acquired in the frequency modulation (FM) mode [35] with an oscillation amplitude of 4 nm. A bias voltage was applied to the sample with respect to the tip. An n-type GaAs(001) wafer with a p-n junction layer on top was cut into pieces with the size of approximately 8 mm $\times$ 3 mm. Each piece was fixed between two metal plates on a sample holder. A voltage can be applied to each metal plate individually. The sample was cleaved at room temperature to obtain a clean GaAs(110) surface and was immediately transferred to the low-temperature SPM head. In the scanning tunneling spectroscopy measurements, the variable tip-sample separation technique was used to ensure a large dynamic range of current detection. The obtained spectra were converted to a constant tip-sample separation by multiplying the measured current by $\exp(2\kappa\Delta z)$, where κ is the decay constant and Δz is the offset of the tip-sample separation [36]. The value of κ was determined experimentally by measuring the tip-sample distance dependence of the tunneling current [36, 37]. A value of 11 nm^{-1} was used for the data presented in this study.

3. Results and discussion

First, STM was performed across the p-n junction to observe the surface properties using a qPlus sensor with a W tip. The measurements were performed on a GaAs(110) surface prepared via cleavage. Figure 1(a) presents a large-scale STM image. The

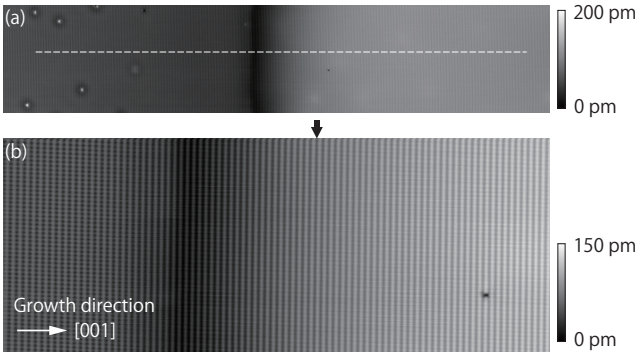

Figure 1. (a) Large-scale (200 nm × 40 nm) constant current topographic images of the GaAs(110) surface obtained across the p-n junction with STM mode. The terminal of the p-n junction is short-circuited. Excitation of the qPlus sensor is turned off during the measurements. Bias voltage and tunneling current are set to −2.2 V and 10 pA, respectively. The dashed line represents the position where the KPFM measurements shown in Fig. 2 were performed. (b) High-resolution topographic images (50 nm × 20 nm) around the p-n junction interface in (a). The arrow indicates the position of the p-n junction interface estimated from the KPFM measurement.

surface was atomically flat, and no steps were observed over a distance of more than 1 μm. Therefore, the surface was considered to have no surface states within the bandgap; thus, the band near the surface was flat [23, 33]. In the middle of the image, a sharp contrast change was observed; however, this position did not coincide with the position of the interface between the p- and n-type layers. The position of the contrast change varies depending on the bias voltage. Figure 1(b) shows a magnified STM image of the p-n junction interface. The p- and n-type layers were continuously connected without any strain or defects. Therefore, estimating the position of the interface using only topographic images was challenging. The arrow above the image indicates the position of the p-n junction interface estimated from the CPD profile described below.

Next, we performed KPFM to characterize the electrostatic potential distribution across the p-n junctions. The qPlus sensor was oscillated with an amplitude of 4.0 nm, and the forces acting between the tip and sample were detected using the shift in the resonance frequency (Δf) of the sensor [35]. Tip-sample separation was controlled using the STM mode. For the KPFM measurements, Δf was measured as a function of the bias voltage (U) at 1024 points on a 180 nm line along the [001] direction, as indicated in Fig. 1(a) (dashed line). Each Δf–U spectrum was fitted with a 2nd-order polynomial (a quadratic function) to derive the bias voltage (U_{CPD}) at which the electrostatic force between the tip and sample was minimized [1]. This method of CPD detection is called Kelvin probe force spectroscopy [38, 39, 40]. This method is equivalent to FM-KPFM [41] and is known to have a smaller tip-averaging effect than amplitude-modulation KPFM [41]. The CPD profile derived by the fitting is shown in Fig. 2(a) (solid blue line). The simulated potential profile is also displayed (dashed black line). The width of the space-charge layer estimated from the CPD profile was in reasonable agreement with

that of the simulation. However, the magnitude of the built-in potential (the potential difference between the p- and n-type layers) was smaller than that in the simulation.

To determine the cause of the discrepancy between the experiment and theory, we analyzed each Δf–U spectrum and the fitting curve. In Fig. 2(b), we show the Δf–U spectrum (gray solid line) obtained at the left end of the 1D measurement line (n-type layer) and the fitting curve (blue dashed line). The discrepancy between the spectrum and fitting was relatively large on the left side of the inflection point. Consequently, the CPD derived from the fitting shifted to the right (higher bias voltage) compared with the bias voltage at which the electrostatic force was minimized. The data obtained in the p-type layer also exhibited a similar shift, although the shift was smaller than that in the n-type layer (see Supplementary Fig. S1). These shifts in the CPD values arising from fitting errors led to a smaller magnitude of the built-in potential than the theoretical value.

Errors in the fitting arise from bias-dependent changes in the tip-sample capacitance. The electrostatic force gradient (F'_{ts}) between the tip and the sample measured by FM-AFM can be expressed as follows [3, 38]:

$$F'_{ts} = \frac{1}{2}\frac{\mathrm{d}^2 C(z,U)}{\mathrm{d}z^2}(U - U_{\mathrm{CPD}})^2, \tag{1}$$

where z is the tip-sample separation and $C(z,U)$ is the tip-sample capacitance. When the tip and sample are metallic, the $C(z,U)$ generally does not depend on U. Therefore, fitting the Δf–U spectrum to a 2nd-order polynomial is physically reasonable for determining the minimum electrostatic force. However, this is not the case for semiconductors, where $C(z,U)$ depends on U because the width of the surface-charging layer near the surface varies depending on the bias voltage [42]. For example, the width of the accumulation layer (formed by the accumulation of charge carriers) is generally smaller than that of the space-charge layer (formed by the depletion of charge carriers and the resultant charging of dopant atoms). The physically important aspect of CPD detection is finding the bias voltage at which the electrostatic force is minimized; fitting with a 2nd-order polynomial is not essential.

To more accurately trace the curvatures near the inflection points of the Δf–U spectra, we attempted fittings using higher-order polynomials. The fitting curve using a 9th-order polynomial is shown in Fig. 2(b) (red dashed line). The errors observed in the 2nd-order polynomial fitting were reduced, particularly on the left side of the inflection point. Consequently, the derived CPD shifted to the left (smaller value) than that derived from the 2nd-order polynomial fitting. The CPD profile obtained from the 9th-order polynomial fittings is shown in Fig. 2(a) (red solid line). The profile was weakly smoothed using a three-point moving average filter to remove the noise discussed below (the raw CPD profile is shown in Supplementary Fig. S2(h)). The magnitude of the built-in potential was in reasonable agreement with the theoretical value. Furthermore, the CPD variation across the space-charge layer reproduced the line shape of the simulated potential well.

Supplementary Fig. S2 shows the dependence of the CPD profile on the order of the

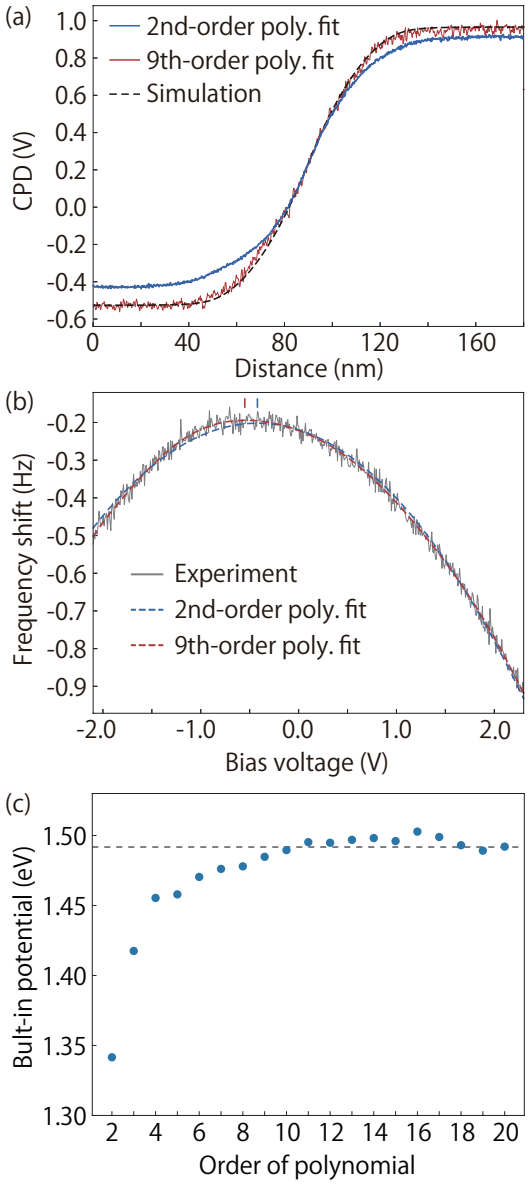

Figure 2. (a) CPD profiles obtained across the p-n junction indicated in Fig. 1(a). The bias voltage and tunneling current were set to −2.4 V and 10 pA, respectively, for STM feedback control. During the Δf–U measurements, the tip was lifted by 100 pm from the set point separation. Blue and red solid lines indicate the CPD profiles derived from 2nd- and 9th-order polynomials, respectively. The dashed black line displays the simulated potential profile, which is offset for comparison with the CPD profiles. (b) Δf–U curve obtained at the left end of the 1D measurement line (gray solid line). Blue and red solid lines show the fitting curves using the 2nd- and 9th-order polynomials, respectively. Vertical lines indicate the inflection points of each polynomial. (c) CPD difference between p-type and n-type layers (built-in potential) plotted as a function of the order of polynomial. The dashed horizontal line indicates the theoretical value of the built-in potential.

polynomial used for fitting. The magnitudes of the built-in potential in the CPD profiles were substantially smaller than the simulated values up to 3rd-order polynomial fitting. For the 4th- and higher-order polynomials, the line shape did not change noticeably and showed reasonable agreement with the simulations. The noise level of the CPD profile increased with increasing fitting order, probably because the increased accuracy of CPD detection made the actual measurement noise more visible.

To evaluate the quantitativity of the CPD measurements in detail, we measured the magnitude of the built-in potential from the CPD difference between the p- and n-type layers. In Fig. 2(c), the magnitude is plotted as a function of the polynomial order from 2 to 20. The CPD difference increases steeply between the 2nd- and 4th-order fitting. Subsequently, it increased gradually up to the 10th-order fitting, when it saturated near the theoretical value. After the 9th-order fitting, the difference from the theoretical value was less than 10 mV. This finding indicates that the decrease in the built-in potential due to the tip-averaging effect is negligible (less than 1 %) and that KPFM using a qPlus sensor AFM can quantitatively measure the potential distributions that vary on the order of 10 nm.

We also measured the changes in the potential distribution induced by light irradiation at the p-n junction. In this measurement, the p-n junction was an open circuit, and the bias voltage was applied to the substrate side (n-type layer side) electrode. The sample and the tip were prepared separately from those used to obtain the data shown in Fig. 2. Figure 3 shows the CPD profiles obtained under dark- and light-irradiation conditions. Light irradiation significantly altered the CPD profiles. The OCV estimated from the CPD change was 535 mV, which was consistent with the OCV (539 mV) obtained from the current-voltage characteristics of the p-n diode (see Supplementary Fig. S3). This result confirmed that the potential distribution could also be quantitatively measured under the device operating conditions.

To further verify the accuracy of our CPD measurements, we performed 1D tunneling spectroscopy across the p-n junction. As the GaAs(110) has no surface states within the band gap, the band edge positions can be estimated by analyzing the onset of the tunneling current (I_t) in I_t–U spectra [36]. For the I_t–U measurement, the variable tip-sample separation technique was used to obtain a large dynamic range of the tunneling current [36]. After the measurement, the I_t–U spectra were converted to a constant tip-sample separation (see the Methods section for the detailed procedure). The applied variation in the tip-sample separation is shown in Supplementary Fig. S4. I_t–U spectra were acquired at 1024 points on a 180 nm line along the [001] direction. In Fig. 4(a), we present a two-dimensional (2D) color map of the absolute tunneling current as a function of the distance (X-axis) and bias voltage (Y-axis). The valence band edge (E_{V}) and conduction band edge (E_{C}) calculated in the simulation are indicated by the yellow dashed lines.

As seen in Fig. 4(a), the onsets of the valence and conduction band components (tunneling out of the valence band states and tunneling into the conduction band states) approximately reproduce the positions of E_{V} and E_{C}, which visualizes the band structure

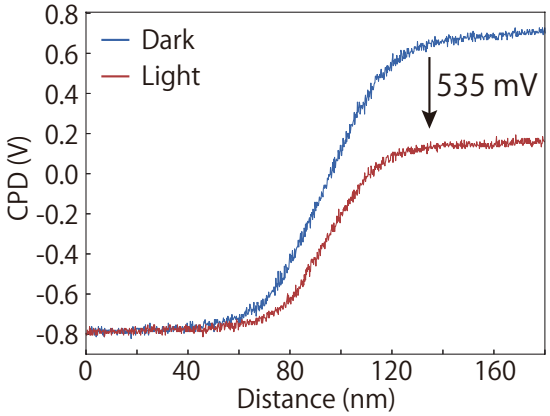

Figure 3. (a) CPD profiles obtained in the open-circuit configuration in the dark and under light-irradiation conditions. A bias voltage was applied to the substrate (n-type layer) side electrode. For the fitting procedures in CPD derivation, the 9th-order polynomial was used. The OCV estimated from the CPD change at the p-type layer was 535 mV.

across the p-n junction. However, some discrepancies were observed. In the regions outside the space-charge layer, the onset of the valence (conduction) band component in the n-type (p-type) layer deviated slightly from the band edges by 50-100 mV (see also I_t–U spectra shown in Supplementary Fig. S4). This was induced by the relatively small current component, called the dopant-induced component (D-component), observed in the bandgap region [43], as explained in Supplementary Fig. S4. In the space-charge-layer region, the onset of the conduction (valence) band component agrees well with E_{C} (E_{V}) around the n-type (p-type) layer side edge. However, the deviations from the theoretical line shape increased toward the p-type (n-type) layer side. Because of these deviations, the apparent bandgap derived from the I_t–U spectra was larger than the actual bandgap. These findings suggest that 1D tunneling spectroscopy can qualitatively visualize the band structure, but is less quantitative than CPD analysis.

Despite its relatively low quantitativity, 1D tunneling spectroscopy provides essential information about the potential reference, that is, the band edge positions relative to the Fermi level. Note that KPFM measurements do not provide a potential reference unless the work function of the tip is determined accurately. Considering these facts, the combined use of 1D tunneling spectroscopy and KPFM is a powerful method for characterizing the quantum semiconductor devices based on III-V materials. In such devices, precise controls and characterizations of some local physical properties, including the electric field, the doping condition, and the Fermi level position, are required for extracting the best device performance [44, 45].

The 2D color map shown in Fig. 4(a) suggests that the D-component is highly sensitive to band bending. The D-component rapidly decreased as soon as the band began to bend near the space-charge layer for both the n-type and p-type layers and completely vanished in the space-charge layer. This is because the charge carriers

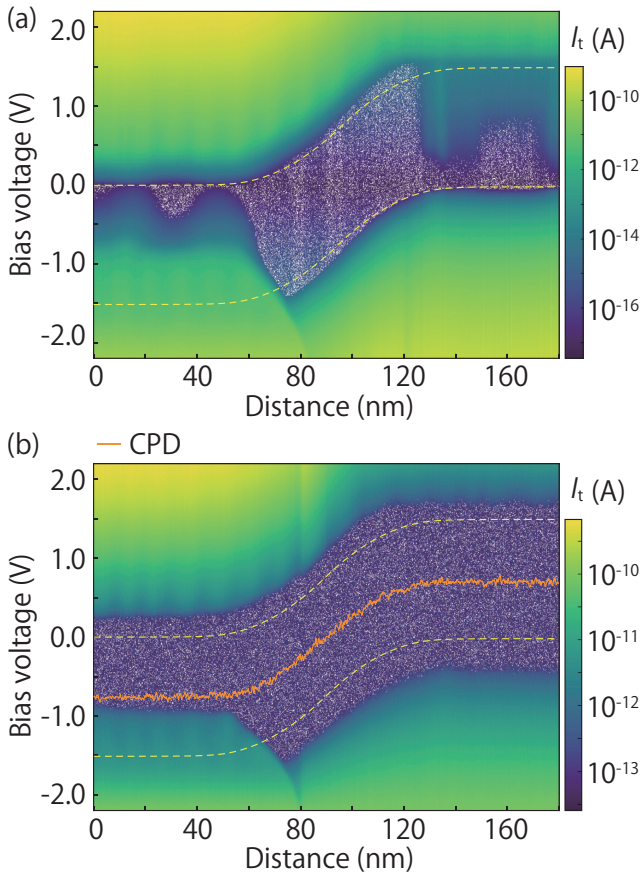

Figure 4. (a) 2D map of 1D tunneling spectroscopy data. The X-axis corresponds to the distance, and the Y-axis corresponds to bias voltage. Excitation of the qPlus sensor is turned off during the measurement. To obtain comparable tunneling current values in both p- and n-type layers, the tip-sample separation at the initial bias point was kept constant along the 1D measurement line. To do this, the tip was moved in the constant height mode without feedback control. The current values below the noise level (20 fA) in the raw data before distance compensation are mapped in white. The positions of E_{V} and E_{C} from the simulation are indicated by yellow dashed lines. (b) 2D map of 1D tunneling spectroscopy data obtained with the constant tip-sample separation mode and CPD profile (orange solid line) derived from simultaneously obtained Δf–U spectra. Tip-sample separation was regulated using the STM mode with a bias voltage of -2.2 V and tunneling current of 10 pA.

(electrons or holes) that contribute to the D-component are depleted because of band bending [46]. We also observed fluctuations in the onset positions of the D-component depending on its location in both the p- and n-type regions outside the space-charge layer. This fluctuation can be explained by slight local potential fluctuations due to the presence of impurities. These findings indicate that analyzing the spatial dependence of the D-component provides strong insights into local band bending and local carrier concentration.

The qPlus sensor AFM enables simultaneous detection of tunneling current and electrostatic forces. Thus, we can directly compare the band structures estimated from

1D tunneling spectroscopy and the CPD profiles at the same location. Figure 4(b) shows a 2D color map of the I_t–U spectra and CPD profile (orange solid line) simultaneously obtained across the p-n junction. For this experiment, the variable tip-sample separation technique could not be used because Δf signals cannot be converted for constant tip-sample separation. Therefore, the apparent bandgap in the 2D color map appears to be larger than the actual bandgap in all regions across the p-n junction. Nevertheless, the shapes of the band edges approximately reproduce the line shapes of E_{C} and E_{V}. Importantly, the line shapes varied almost parallel to the CPD profile. This result also supports the fact that KPFM accurately measured the electrostatic potential distribution across the p-n junction.

4. Summary

In summary, our results demonstrate the effectiveness of KPFM measurements using qPlus sensor AFM for characterizing the electrostatic potential distributions formed in semiconductor devices. We demonstrated that, for a semiconductor surface, the use of a higher-order polynomial instead of a 2nd-order one (a quadratic function) in the fitting procedure improves the accuracy of CPD detection. The CPD profile obtained by the fittings across the p-n junction reproduced well not only the magnitude of the built-in potential but also the change in the potential across the space-charge layer. We also succeeded in measuring the open-circuit voltage of the p-n diode by detecting changes in the CPD profiles upon light irradiation. In addition to the KPFM measurements, we demonstrated that 1D tunneling spectroscopy using the variable tip-sample separation technique could visualize the band structure across the p-n junction. The simultaneous 1D tunneling spectroscopy and KPFM measurements provided evidence that the band edge position and CPD profile varied similarly. All these measurements demonstrate that the KPFM measurements using qPlus sensor AFM can quantitatively measure the potential distribution, whose change occurs on the order of 10 nm. Our results also provide a basis for the future evaluation of quantum semiconductor devices based on III-V semiconductors using STM, AFM, and KPFM.

Acknowledgments

We would like to thank T. Noda for valuable discussions. This work was partially supported by JSPS KAKENHI Grant Numbers JP17K06366 and JP21H01818.

References

[1] Nonnenmacher M, O'Boyle M P and Wickramasinghe H K 1991 *Applied Physics Letters* **58** 2921–2923
[2] Melitz W, Shen J, Kummel A C and Lee S 2011 *Surface Science Reports* **66** 1–27
[3] Sadewasser S and Glatzel T (eds) 2012 *Kelvin Probe Force Microscopy: Measuring and Compensating Electrostatic Forces* (Springer)

[4] Glatzel T, Gysin U and Meyer E 2022 *Microscopy* **71** i165–i173
[5] Kikukawa A, Hosaka S and Imura R 1995 *Applied Physics Letters* **66** 3510–3512
[6] Shikler R, Meoded T, Fried N and Rosenwaks Y 1999 *Applied Physics Letters* **74** 2972–2974
[7] Robin F, Jacobs H, Homan O, Stemmer A and Bächtold W 2000 *Applied Physics Letters* **76** 2907–2909
[8] Glatzel T, Sadewasser S, Shikler R, Rosenwaks Y and Lux-Steiner M 2003 *Materials Science and Engineering: B* **102** 138–142
[9] Minj A, Cros A, Auzelle T, Pernot J and Daudin B 2016 *Nanotechnology* **27** 385202
[10] Cai M, Ishida N, Li X, Yang X, Noda T, Wu Y, Xie F, Naito H, Fujita D and Han L 2018 *Joule* **2** 296–306
[11] Noda T, Ishida N, Mano T and Fujita D 2020 *Applied Physics Letters* **116** 163501
[12] Nakamura T, Ishida N, Sagisaka K and Koide Y 2020 *AIP Advances* **10** 085010
[13] Hiraoka M, Ishida N, Matsushita A, Uchida R, Sekimoto T, Yamamoto T, Matsui T, Kaneko Y, Miyano K, Yanagida M and Shirai Y 2022 *ACS Applied Energy Materials* **5** 4232–4239
[14] Zhu J, Zeng K and Lu L 2012 *Journal of Applied Physics* **111** 063723
[15] Luchkin S Y, Amanieu H Y, Rosato D and Kholkin A L 2014 *Journal of Power Sources* **268** 887–894
[16] Masuda H, Ishida N, Ogata Y, Ito D and Fujita D 2017 *Nanoscale* **9**(2) 893–898
[17] Masuda H, Matsushita K, Ito D, Fujita D and Ishida N 2019 *Communications Chemistry* **2** 140
[18] Otoyama M, Yamaoka T, Ito H, Inagi Y, Sakuda A, Tatsumisago M and Hayashi A 2021 *The Journal of Physical Chemistry C* **125** 2841–2849
[19] Ishida N 2022 *Beilstein Journal of Nanotechnology* **13** 1558–1563
[20] Chavez-Pirson A, Vatel O, Tanimoto M, Ando H, Iwamura H and Kanbe H 1995 *Applied Physics Letters* **67** 3069–3071
[21] Jiang C S, Moutinho H R, Friedman D J, Geisz J F and Al-Jassim M M 2003 *Journal of Applied Physics* **93** 10035–10040
[22] Gysin U, Glatzel T, Schmölzer T, Schöner A, Reshanov S, Bartolf H and Meyer E 2015 *Beilstein Journal of Nanotechnology* **6** 2485–2497
[23] Mönch W 2001 *Semiconductor Surfaces and Interfaces, Third edition* (Springer)
[24] Zhang Z and Yates J T J 2012 *Chemical Reviews* **112** 5520–5551 pMID: 22783915
[25] Fuller E J, Pan D, Corso B L, Tolga Gul O, Gomez J R and Collins P G 2013 *Applied Physics Letters* **102** 083503
[26] Panchal V, Pearce R, Yakimova R, Tzalenchuk A and Kazakova O 2013 *Scientific Reports* **3** 2597
[27] Wagner T, Beyer H, Reissner P, Mensch P, Riel H, Gotsmann B and Stemmer A 2015 *Beilstein Journal of Nanotechnology* **6** 2193–2206
[28] Axt A, Hermes I M, Bergmann V W, Tausendpfund N and Weber S A L 2018 *Beilstein Journal of Nanotechnology* **9** 1809–1819
[29] Jiang C S, Friedman D J, Geisz J F, Moutinho H R, Romero M J and Al-Jassim M M 2003 *Applied Physics Letters* **83** 1572–1574
[30] Baumgart C, Helm M and Schmidt H 2009 *Phys. Rev. B* **80**(8) 085305
[31] Giessibl F J 2000 *Applied Physics Letters* **76** 1470–1472
[32] Giessibl F J 2019 *Review of Scientific Instruments* **90** 011101
[33] van Laar J, Huijser A and van Rooy T L 1977 *Journal of Vacuum Science and Technology* **14** 894–898
[34] Semitip version 6, https://www.andrew.cmu.edu/user/feenstra/
[35] Albrecht T R, Grütter P, Horne D and Rugar D 1991 *Journal of Applied Physics* **69** 668–673
[36] Feenstra R M 1994 *Phys. Rev. B* **50**(7) 4561–4570
[37] Ishida N, Sueoka K and Feenstra R M 2009 *Phys. Rev. B* **80**(7) 075320
[38] Vančura T, Kičin S, Ihn T, Ensslin K, Bichler M and Wegscheider W 2003 *Applied Physics Letters* **83** 2602–2604
[39] Münnich G, Donarini A, Wenderoth M and Repp J 2013 *Phys. Rev. Lett.* **111**(21) 216802

[40] Albrecht F, Fleischmann M, Scheer M, Gross L and Repp J 2015 *Phys. Rev. B* **92**(23) 235443
[41] Zerweck U, Loppacher C, Otto T, Grafström S and Eng L M 2005 *Phys. Rev. B* **71** 125424
[42] Schwarz A, Allers W, Schwarz U D and Wiesendanger R 2000 *Phys. Rev. B* **62**(20) 13617–13622
[43] Feenstra R M and Stroscio J A 1987 *Journal of Vacuum Science and Technology B: Microelectronics Processing and Phenomena* **5** 923–929
[44] Otsubo K, Hatori N, Ishida M, Okumura S, Akiyama T, Nakata Y, Ebe H, Sugawara M and Arakawa Y 2004 *Japanese Journal of Applied Physics* **43** L1124
[45] Watanabe K, Asahi S, Zhu Y and Kita T 2021 *Journal of Applied Physics* **130** 085701
[46] Feenstra R M, Yu E T, Woodall J M, Kirchner P D, Lin C L and Pettit G D 1992 *Applied Physics Letters* **61** 795–797